RESEARCH ARTICLE
SPACE PHYSICS

Earth and Planetary Physics
10: 144–155, 2026
doi: 10.26464/epp2026013

Tracing equatorward and poleward boundaries of the magnetospheric cusp from a simulated X-ray image

Xue Wang[1,2,3], TianRan Sun[1*], C. Philippe Escoubet[4], Andy Read[5], YiHong Guo[6], Steve Sembay[5], and Chi Wang[1,2]

[1]National Space Science Center, Chinese Academy of Sciences, Beijing 100190, China;

[2]College of Earth and Planetary Sciences, The University of Chinese Academy of Sciences, Beijing 100149, China;

[3]Laboratoire de Physique des Plasmas (LPP), CNRS, E cole Polytechnique, Sorbonne Universite, Universit e Paris-Saclay, Observatoire de Paris, 91120 Palaiseau, France;

[4]European Space Agency/European Space Research and Technology Centre, Noordwijk, The Netherlands;

[5]Department of Physics and Astronomy, University of Leicester, Leicester, United Kingdom;

[6]Aerospace Information Research Institute, Chinese Academy of Sciences, Beijing 100094, China

Key Points:

- Equatorward and poleward boundaries of the cusp were traced from a simulated image of X-ray intensity.
- The effect of interplanetary magnetic field B_z was analyzed in the simulated X-ray image.
- An X-ray photon count image obtained by instrument simulation was used to validate the method of boundary tracing.

Citation: Wang, X., Sun, T. R., Escoubet, C. P., Read, A., Guo, Y. H., Sembay, S., and Wang, C. (2026). Tracing equatorward and poleward boundaries of the magnetospheric cusp from a simulated X-ray image. *Earth Planet. Phys.*, *10*(1), 144–155. http://doi.org/10.26464/epp2026013

Abstract: A large-scale view of the magnetospheric cusp is expected to be obtained by the Soft X-ray Imager (SXI) onboard the Solar wind Magnetosphere Ionosphere Link Explorer (SMILE). However, it is challenging to trace the three-dimensional cusp boundary from a two-dimensional X-ray image because the detected X-ray signals will be integrated along the line of sight. In this work, a global magnetohydrodynamic code was used to simulate the X-ray images and photon count images, assuming an interplanetary magnetic field with a pure B_z component. The assumption of an elliptic cusp boundary at a given altitude was used to trace the equatorward and poleward boundaries of the cusp from a simulated X-ray image. The average discrepancy was less than 0.1 R_E. To reduce the influence of instrument effects and cosmic X-ray backgrounds, image denoising was considered before applying the method above to SXI photon count images. The cusp boundaries were reasonably reconstructed from the noisy X-ray image.

Keywords: SMILE mission; X-ray image; cusp boundary

1. Introduction

The polar cusp, an important region of Earth's magnetosphere, provides a channel for solar wind particles to enter the magnetosphere and ionosphere. In response to solar wind variations, the cusp boundary changes on a large scale. Initially, Chapman and Ferraro (1930) considered the cusp a special region where the geomagnetic field was zero. Later, the cusp was recognized as a region of open magnetic field lines that allowed plasma from the magnetosheath to enter directly (Frank, 1971; Heikkila and Winningham, 1971). The cusp is defined as a localized region near noon with plasma spectral properties closer to the original magnetosheath (Newell et al., 1989). It is filled mostly by plasma from the magnetosheath and a small amount of plasma from the ionosphere (Fuselier et al., 2001; Sawyer et al., 2021). The cusp region has been defined in different ways for different research questions. Although researchers who have focused on different questions have defined the cusp region differently, all agree on the following physical characteristics: (1) It is a special area where the Earth's magnetic field is significantly reduced at the magnetopause (Lavraud et al., 2002; Zong QC et al., 2004); (2) the region allows the solar wind to enter directly, and a small number of ionospheric particles can rise from there, making it an important region for the solar wind–magnetosphere–ionosphere coupling (Newell and Meng, 1988; Newell et al., 1989; Zhou XW et al., 2000; Cargill et al., 2005; Escoubet et al., 2013).

Abundant local information about the cusp boundary and its physical processes can be obtained through *in situ* observations. Such observations can be categorized into three groups based on cusp altitude: low-, mid-, and high-altitude cusp regions. At low altitudes, observations from satellites and rockets have yielded information regarding cusp characteristics and the control of the solar wind on the cusp boundary (Reiff et al., 1977; Escoubet and Bosqued, 1989; Newell et al., 1989; Zhou XW et al., 2000; Fritz and

First author: X. Wang, wangxue@spaceweather.ac.cn
Correspondence to: T. R. Sun, trsun@swl.ac.cn
Received 24 DEC 2024; Accepted 13 OCT 2025.
First Published online 19 NOV 2025.

Zong Q-G, 2005; Watermann et al., 2005; Fritz et al., 2020; Petrinec et al., 2023). Mid-altitude cusp structure and dynamics have been observed by Cluster, Polar, and DE-1 (Dynamic Explorer 1); these data have revealed coupling between the solar wind and the cusp (Burch, 1988; Pitout et al., 2006, 2009; Escoubet et al., 2008, 2013; Bogdanova et al., 2020; Pitout and Bogdanova, 2021). The high-altitude cusp has been explored by ISIS 1 (International Satellites for Ionospheric Studies 1; Heikkila and Winningham, 1971), IMP5 (Interplanetary Monitoring Platform 5; Frank, 1971), Ogo 5 (Russell et al., 1971), Polar (André and Yau, 1997), and Cluster (Escoubet et al., 2001; Dunlop et al., 2005; Lavraud et al., 2005). In this region, the cusp is highly dynamic, with magnetic field disturbance, turbulence, and high-energy particles possibly observed (Scarf et al., 1972; Burch, 1973; Měrka et al., 2002; Bogdanova et al., 2005; Cai HT et al., 2010; Pitout and Bogdanova, 2021). On the basis of a statistical analysis of many cusp crossing events from low- to high-altitude satellites, such as DMSP (Defense Meteorological Satellite Program; Newell and Meng, 1988; Newell et al., 1989), Polar (Zhou XW et al., 2000), and Cluster (Pitout et al., 2006; Xiao C et al., 2018), it has been feasible to roughly outline the large-scale morphology of the cusp. Empirical models of the magnetopause depression and cusp boundary have also been created by statistical analysis (Tsyganenko and Russell, 1999; Lin RL et al., 2010; Xiao C et al., 2018).

The influence of the interplanetary magnetic field (IMF) on the cusp has been widely studied. Among the three components, IMF B_z plays the most dominant role in determining the latitudinal position of the cusp. For northward ($B_z > 0$), the cusp boundary is relatively poleward, whereas after IMF southward turning, it shifts equatorward. These results are largely consistent across both case and statistical studies (Newell et al., 1989; Zhou X-W et al., 1999; Cao JB et al., 2005; Trattner et al., 2005, 2011; Pitout et al., 2006, 2021). In comparison, the effects of IMF B_y are more variable, often associated with cusp shifts in the Magnetic Local Time (MLT) direction (Newell et al., 1989; Zhou X-W et al., 1999; Zhang B et al., 2013; Liu ZQ et al., 2015). The influence of IMF B_x has rarely been explored, with only limited investigations suggesting possible effects (Xu JY et al., 2018). In addition to the IMF, the Earth's dipole tilt angle affects the cusp position—generally, a larger tilt angle leads to a more poleward shift of the cusp (Zhou X-W et al., 1999; Pitout et al., 2006; Liu ZQ et al., 2012).

Despite various investigations thus far, *in situ* satellite observations have limited coverage at different altitudes because of the satellite orbit settings. It is also difficult to distinguish temporal and spatial changes based on *in situ* observations, although this is possible under some special circumstances (Trattner et al., 2002; Escoubet et al., 2008; Zong Q-G et al., 2008). Recent advances in soft X-ray imaging of the magnetosphere have now made it possible to study large-scale structures of the cusp region. Telescopes onboard astronomical satellites have observed this phenomenon by using narrow field-of-view (FOV) technology (e.g., Fujimoto et al., 2007; Carter et al., 2010). With an X-ray imager featuring a wide FOV, such as the SXI onboard the Solar wind Magnetosphere Ionosphere Link Explorer (SMILE), it is possible to capture images of the line-of-sight (LOS) integrations of solar wind charge exchange (SWCX) X-rays. It will be able to see a large-scale cusp structure at different altitudes, which was not possible in the prior observations. These images carry vital information about the magnetopause or cusp boundary (Sun TR et al., 2015, 2019). The magnetopause and cusp region, where the interactions between the solar wind and magnetosphere are particularly intense, demonstrate significantly higher SWCX levels than the surrounding areas (Sun TR et al., 2019; Branduardi-Raymont et al., 2021; Wang C et al., 2025). Consequently, the magnetopause and cusp information derived from an X-ray image of the magnetosphere is of considerable interest (see the simulations from the SMILE Modeling Working Group: Grandin et al., 2024; Guo J et al., 2024; Kim et al., 2024; Samsonov et al., 2024; Yang ZW et al., 2024; Connor et al., 2025, among others).

Sun TR et al. (2019) have simulated soft X-ray images of the magnetopause and cusp region. Various methods have been proposed to reconstruct the magnetopause boundary from X-ray images, such as the boundary fitting approach (BFA; Jorgensen et al., 2019, 2022), tangent fitting approach (TFA; Sun TR et al., 2020), tangential direction approach (TDA; Collier and Connor, 2018), and computed tomography approach (CTA; Wang C and Sun TR, 2022). Guo YH et al. (2022) traced the magnetopause boundary from X-ray photon count images by considering the SXI instrument effect and the diffusive cosmic background. On the basis of a magnetohydrodynamic (MHD) simulation, Sun TR et al. (2021) derived the tangent directions of the cusp in a simulated X-ray image.

From the studies mentioned previously, we have learned that the cusp is a region characterized by significant disturbances in terms of its position and size, influenced by the solar wind plasma and IMF conditions. To further derive the large-scale boundaries of the cusp region, and in particular the equatorward and poleward boundaries, from X-ray images of the cusp, we apply a new boundary tracing method. On the basis of an MHD simulation, a hypothetical satellite observes the X-ray image of the cusp region from a dawn-side location. In Section 3, the equatorward and poleward boundaries are analyzed from the simulated X-ray image. This method is further validated under different IMF B_z by investigating the effect of B_z on the boundaries in the simulated X-ray image. Section 4 presents the cusp boundary results in simulated photon count images when the influence of the SXI instrument noise and background cosmic X-rays have been taken into consideration. Section 5 presents and discusses conclusions drawn from the study.

2. Data and Methods

2.1 MHD Simulation and X-ray Intensity Model

Global MHD simulations have been successful in describing the large-scale structures and overall evolutions in the solar wind–magnetosphere coupling system. The global MHD model used in this study is the piecewise parabolic method with a Lagrangian remap (PPMLR-MHD) developed by Hu YQ et al. (2007). This model provides the interactions between the solar wind, magnetosphere, and ionosphere. It can provide basic physical parameters in three-dimensional (3D) space, including plasma density, plasma velocity components, magnetic field components, and pressure.

The code solves MHD equations in Geocentric Solar Magnetospheric (GSM) coordinates ($-100 < X < 30\ R_E$, $-100 < Y < 100\ R_E$, $-100 < Z < 100\ R_E$), with an inner boundary at $r = 3\ R_E$. From this inner shell to the ionosphere, the field-aligned current and electric field are coupled along the dipole field. The ionosphere is treated as a spherical shell, with constant conductance.

This study involves X-ray images under three solar wind conditions, with the parameters listed in Table 1. The solar wind number densities used in this article are higher than average because the SMILE mission is designed to observe the magnetosphere under disturbed solar wind conditions (Sembay et al., 2024).

Table 1. Solar wind conditions for the studied simulations.[a]

Run	Number density (cm^{-3})	Velocity (km/s)	B_z (nT)
1	20	400	−5
2	12.5	400	5
3	12.5	400	−5

[a]All IMF B_y and B_x values are set to 0 nT.

The boundaries of the cusp in MHD simulations are identified by the thermal pressure contour lines within the polar region on each spherical shell at a given altitude (Sun TR et al., 2019). Specifically, the cusp boundary is identified as the location where the thermal pressure drops to 60% of the maximum value p_{max} on each shell with a constant altitude (Sun TR et al., 2021). Because the thermal pressure drops rapidly near the boundary, other thresholds, such as 50% or 70%, do not change the main conclusion of this article. The X-ray emissions outside the determined cusp boundary in the MHD have been set to zero, a masking process commonly used in X-ray studies (e.g., Samsonov et al., 2022). In the MHD simulations, the cusp boundary tends to correspond to the cusp proper in observational data, marking the region where the bulk of the plasma accelerated via magnetopause reconnection starts to arrive.

In the FOV of an X-ray imager, the soft X-ray intensity generated by SWCX is related to the solar wind flux (Cravens, 2000; Zhang YJ et al., 2022). It can be calculated using the following equation (Sun TR et al., 2019):

$$I_X = \frac{1}{4\pi}\int P_X dr = \frac{1}{4\pi}\int \alpha_X n_H n_{sw}\sqrt{u_{sw}^2 + u_{th}^2}\,dr, \quad (1)$$

where I_X is in keV cm^{-2} s^{-1} sr^{-1}, P is the local volume emissivity of soft X-rays; α is the interaction efficiency factor, which is set as 6×10^{-16} eV cm^2 in this study (Jorgensen et al., 2019); n_H and n_{sw} are the number densities of exospheric hydrogen atoms and solar wind protons, respectively; u_{sw} is the velocity of the solar wind; and u_{th} is the plasma thermal speed (Sun TR et al., 2015). The n_{sw}, u_{sw}, and n_{th} are obtained from the MHD results, and $n_H = n_0\ (10\ R_E/r)^3\ cm^{-3}$, where $n_0 = 25\ cm^{-3}$ (Cravens, 2000; Connor and Carter, 2019; Fuselier et al., 2020; Sibeck et al., 2021). Several other models can be used to estimate the density of neutral hydrogen (e.g., Zoennchen et al., 2011). In this work, we apply the r^{-3} model for simplicity, as the main focus here is the variation patterns of X-ray intensity near the cusp boundaries, not those affected by different exospheric models.

2.2 MHD X-ray Images and SXI Count Images

On the basis of the LOS integration of the X-ray emissivity in 3D space, an expected X-ray image can be derived within the FOV of the ideal SXI (Sun TR et al., 2019, 2021). The SXI photon count images are simulated based on the MHD result (Guo YH et al., 2022; Sembay et al., 2024) by treating each pixel of the MHD X-ray image as a point source. To collect enough photons in each pixel, the SXI instrument has its pixel resolution set to 0.5° × 0.5° ($\theta \times \phi$) on the image plane. Here, θ–ϕ is the image coordinate system. The direction at (0, 0) shows the telescope pointing direction; the positive θ is oriented toward the Sun; and the ϕ axis is perpendicular to the θ axis (Sun TR et al., 2021). The basic optic parameters of the SXI used in the instrument simulation are shown in Table 2. A 60° × 60° FOV was utilized for the simulation in this methodological study, a field significantly larger than the actual FOV (16° × 27°) of the SXI instrument on SMILE (Branduardi-Raymont et al., 2024; Wang C et al., 2017). This is because only part of the cusp boundary can be seen by SMILE, whereas it is better to know which part of the cusp is visible in the FOV. As can be seen in the following figure (i.e., Figure 4c), sometimes limited portions of both boundaries are visible (for instance, the southward IMF), whereas at other times, only the equatorward boundary is visible.

Table 2. Parameters of the SXI.

Parameter	Value
Optic FOV	60° × 60°
Optic focal length	300 mm
Width of microchannel	40 μm
Thickness of microchannel	6 μm
Length of microchannel	1.2 mm
Optic coating	Iridium
Surface roughness	0.5 nm

The X-ray imaging system of SMILE's SXI utilizes a lobster eye geometry and glass microchannel plates, which reflect X-rays to form images. These microchannel plates, lined with metal-coated walls, direct X-rays to a central point spread function on its arms, affecting the image resolution and detail of the eye. The effective area of the SXI also varies spatially, described by a vignetting function. Optical vignetting is a reduction of an image's brightness toward the periphery compared with the image center, usually caused by the physical dimensions of a multiple-element lens. The vignetting function of the SMILE SXI will be carefully measured during the calibration of the SXI and provided to the public after launch. Thus, instrumental influences on the obtained images must be considered. Our imaging process considers Poisson noise as the number of photons actually counted in a time interval follow a Poisson distribution, assuming a constant X-ray flux in an integration interval and a random time of arrival for individual photons (typical assumptions in imaging). The image has an overall reduced resolution of approximately 6 arc minutes. Additionally, the CCD detector system of the SXI, which is sensitive to the 0.2 to

5 keV energy band, dictates the range of detectable X-ray emissions (Peng SW et al., 2018; Guo YH et al., 2022).

The instrument simulator mainly traces the path of an incident ray by considering the design of the SMILE SXI (Peng SW et al., 2018). Specifically, many incident X-rays are launched according to the input (different distribution patterns of MHD-simulated X-ray intensity). Following the design about the reflective wall of the microchannel, radius of the curvature, size of the microchannel (width, length, and thickness), internal surface, and so forth, a certain ratio exists for each of the X-rays passing the system and being focused on the focal point. Using the Monte Carlo ray-tracing model, we converted the source X-ray intensity to the photon counts expected to be observed by the designed instrument. The instrument effects, such as different focal lengths, the distribution of microchannels, and so forth, could thus be considered.

The diffusive cosmic X-ray background is the primary X-ray background component. Derived from ROSAT All-Sky Survey data, the intensity of this noise is estimated to be roughly 50 keV s^{-1} cm^{-2} sr^{-1} in the SMILE SXI FOV. The instrument simulator calculates the expected foreground (MHD prediction from Equation (1)) and background input components (a uniform background intensity of 50 keV s^{-1} cm^{-2} sr^{-1}), passes through the instrument response (considering the instrument effects, including the point spread function and vignetting function), and then adds the Poisson noise to derive the total counts expected to be observed by SMILE (Sembay et al., 2024).

Other noise sources could also include the Lyman alpha scattering from the exosphere at lower altitudes. Nevertheless, the SMILE SXI straylight system is designed to efficiently suppress the ultraviolet band, including the aluminum optical blocking filter over the SXI optics, so that it has a negligible impact on typical SXI operations.

2.3 Tangent Direction of the Cusp Boundary

Sun TR et al. (2021) indicated that the directions with sudden increases of I_X correspond to the tangent directions of the cusp boundary. Specifically, it is suggested that the sudden variation of local standard deviations in X-ray intensities can be used to determine the tangent directions of the cusp boundary. The definition of local standard deviation σ is as follows:

$$\sigma_k = \sqrt{\frac{1}{3}\sum_{i=0}^{2}\left(I_{x_{k-1+i}} - \bar{I}_{x+k}\right)^2}, \qquad \bar{I}_{x+k} = \frac{1}{3}\left(I_{x_{k-1}} + I_{x_k} + I_{x_{k+1}}\right), \tag{2}$$

where I_k corresponds to the X-ray intensity of point k, whereas k stands for each data point along the ϕ axis, as shown in Figure 1c. The standard deviation for three consecutive numbers is calculated, $k-1$, k, and $k+1$, which corresponds to $k-1+i$ with i running from 0 to 2. Near the boundary of the cusp is a significant enhancement in the X-ray intensity. Therefore, the local standard deviation for identifying the cusp boundary can be selected with a 50% threshold, that is, $\sigma_k \geq \sim 50\%\ \sigma_{max}$, where σ_{max} is the maximum value of σ for each given θ. Because the local standard deviation shows a sharp enhancement at the cusp boundary (Sun TR et al., 2019), changing the threshold results in a negligible difference in the boundary position (<0.05°).

3. Reconstructing the Poleward and Equatorward Boundaries

3.1 Deriving Tangent Directions of the Cusp Boundary

In this section, we describe how we used an ideal SXI located on the dawn side to simulate an X-ray image of the cusp (see Run 1 in Table 1 for the solar wind conditions). The tangent directions of the cusp boundary in the FOV are then identified by the method of local standard deviation (Sun TR et al., 2021), and the results are compared with the equatorward and poleward boundaries of the cusp derived from the MHD simulation on the noon–midnight meridian plane (i.e., the *XOZ* plane in the GSM coordinate system).

SMILE will operate on a large elliptical orbit with a high inclination angle. Sun TR et al. (2021) analyzed the azimuthal boundaries of the cusp from simulated SXI images. To observe the equatorward and poleward cusp boundaries, the satellite is set at a typical dawn-side location. Figures 1a1 to 1a3 depict the relative position of the satellite to the Earth and the cusp region in the *XOY*, *XOZ*, and *YOZ* planes. Figure 1b shows the location of the cusp in the FOV of the satellite's SXI. The blue circle denotes the Earth; the orange and red arcs represent the subsolar magnetopause and cusp boundaries, respectively. The cusp boundary was determined by the T96 model using the poleward and equatorward boundaries from Newell et al. (1989). The SXI position is (5.71, −9.19, 3.95) R_E in the GSM coordinate system, with an FOV of 60° × 60° aimed toward (4.96, −0.39, 1.55) R_E, that is, pointing from (5.71, −7.93, 6.09) to (4.96, 0, 1.60) R_E in Geocentric Solar Ecliptic (GSE) coordinates. The satellite is located at the dawn side with a relatively large *Y* coordinate, which provides a good dawn-side view of the cusp. Figure 1c shows the simulated X-ray image of the cusp derived from MHD simulations, hereafter abbreviated as "the X-ray image." The red line in Figure 1c marks the tangent directions of boundaries identified by the local standard deviation method proposed by Sun TR et al. (2021).

Satellites in the dawn sector can provide a unique perspective for studying the cusp structure (see Figure 1c); thus, we can expect valuable insights into the structure and dynamics of the poleward and equatorward boundaries of the cusp. Latitudinal positions of the 3D cusp boundaries are dependent on longitudes, and more attention is usually paid to the poleward and equatorward boundaries in the noon–midnight meridian plane (the main focus of this article) for cases with small IMF B_y because they define the maximum latitudinal range that the cusp can cover. Nevertheless, the red lines derived directly from the X-ray image in Figure 1c are not the desired ones that define the maximum latitudinal range of the cusp. They merely show the tangent direction of the cusp boundary. A new method must be developed to derive the information on poleward and equatorward boundaries from an X-ray image.

3.2 Fitting the Cusp Boundary Through Tangent Directions

Although the tangent directions can be derived from an X-ray

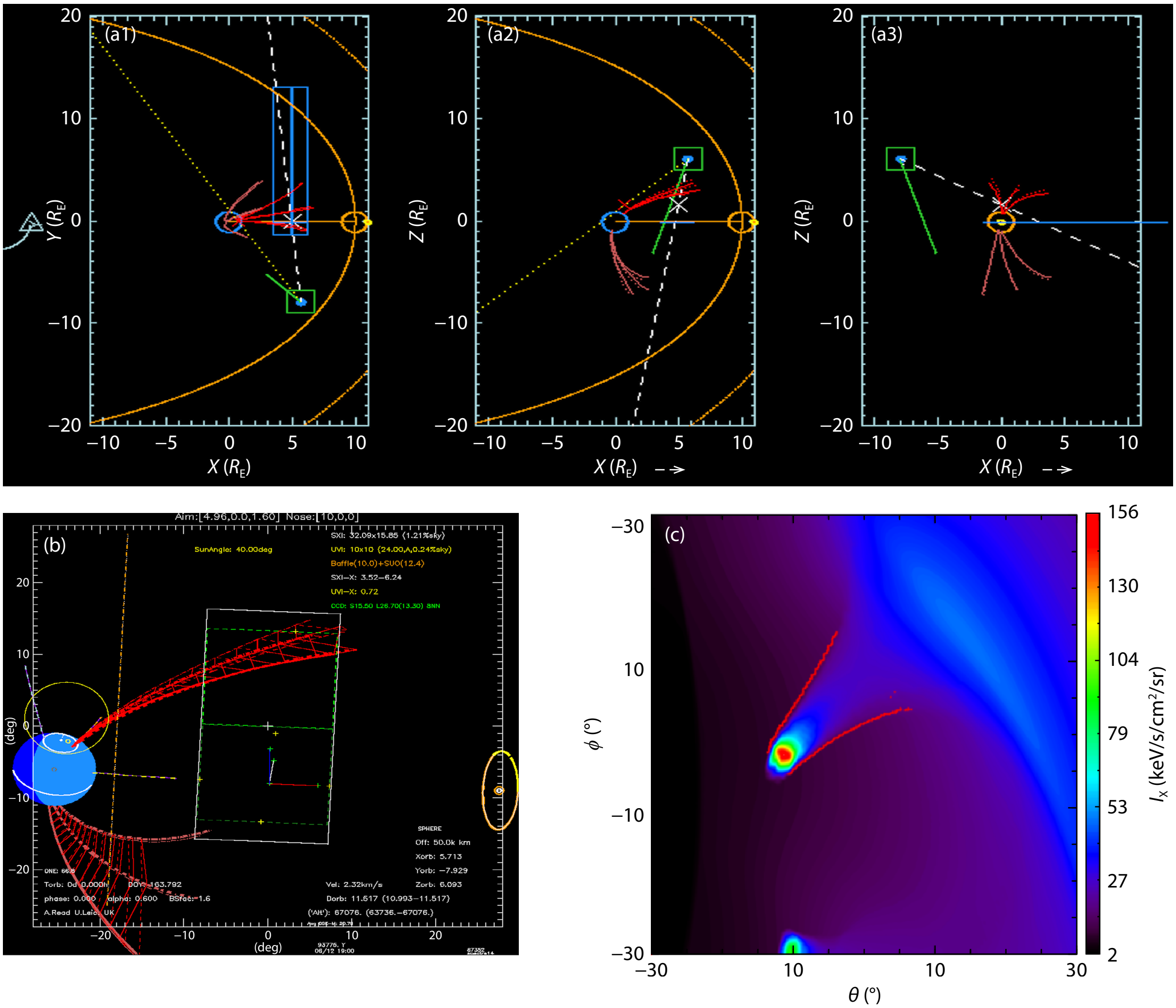

Figure 1. (a1–a3) The satellite position in the *XOY* plane, *XOZ* plane, and *YOZ* plane in GSE coordinates, respectively. The blue dot inside the green rectangle is the location of the satellite. (b) The cusp boundaries, obtained from the T96 model inside the FOV of the SXI on SMILE (the dashed green rectangle). The blue circle represents the Earth; the orange curve is the magnetopause; and the red curves are cusp boundaries from the T96. (c) The MHD-simulated X-ray image of the cusp, and the tangent directions (red lines) derived from the simulation.

image, simply extending these tangent directions does not yield an accurate prediction of the poleward and equatorward boundaries of the cusp, as illustrated in Figures 2a and 2b. The yellow star marks the position of SMILE, and the light blue tunnel-shaped cone illustrates the cusp region. The cone is bright in the soft X-ray band; thus, viewing from the satellite, the X-ray image in Figure 1c can be obtained. The two red lines in Figure 1c correspond to the two yellow lines in Figure 2a and 2b, which are the tangent directions of the cusp. The intersection points of these tangent directions with the noon–midnight meridian plane, marked by the two red dots, deviate from the actual poleward and equatorward boundaries of the cusp in the midnight meridian plane. This offset results from the spacecraft's position relative to the boundary as well as three-dimensional perspective effects. This discrepancy is also evident in Figure 2c, where the dotted red lines indicate the intersections of the tangent directions with the noon–midnight meridian plane and the blue crosses mark the equatorward and poleward boundaries of the MHD cusp. Therefore, it is necessary to develop a method that can more accurately derive the cusp boundaries.

Sun TR et al. (2019) indicated that the cusp boundaries at mid and low altitudes can be approximated as ellipses on each spherical shell at a certain altitude. Therefore, the cusp boundary could be fitted by an elliptic function. A coordinate system was defined to describe its position on the shell, referred to as the cusp coordinate system (Figure 2a): The X_{shell} axis is defined by the intersection line of the XOZ_{GSM} plane with the spherical shell; the Y_{shell} axis is perpendicular to the X_{shell} axis. The equation for each ellipse is

$$\frac{x^2}{a^2} + \frac{y^2}{a^2(1-e^2)} = 1, \tag{3}$$

where a is the long axis and e is eccentricity. The flow diagram for cusp reconstruction is depicted in Figure 3. First, a location with a sudden enhancement of intensity is found from an X-ray image, marking the tangent direction of the cusp boundary (Figure 1c). A model of the cusp boundary is then assumed, which is an ellipse

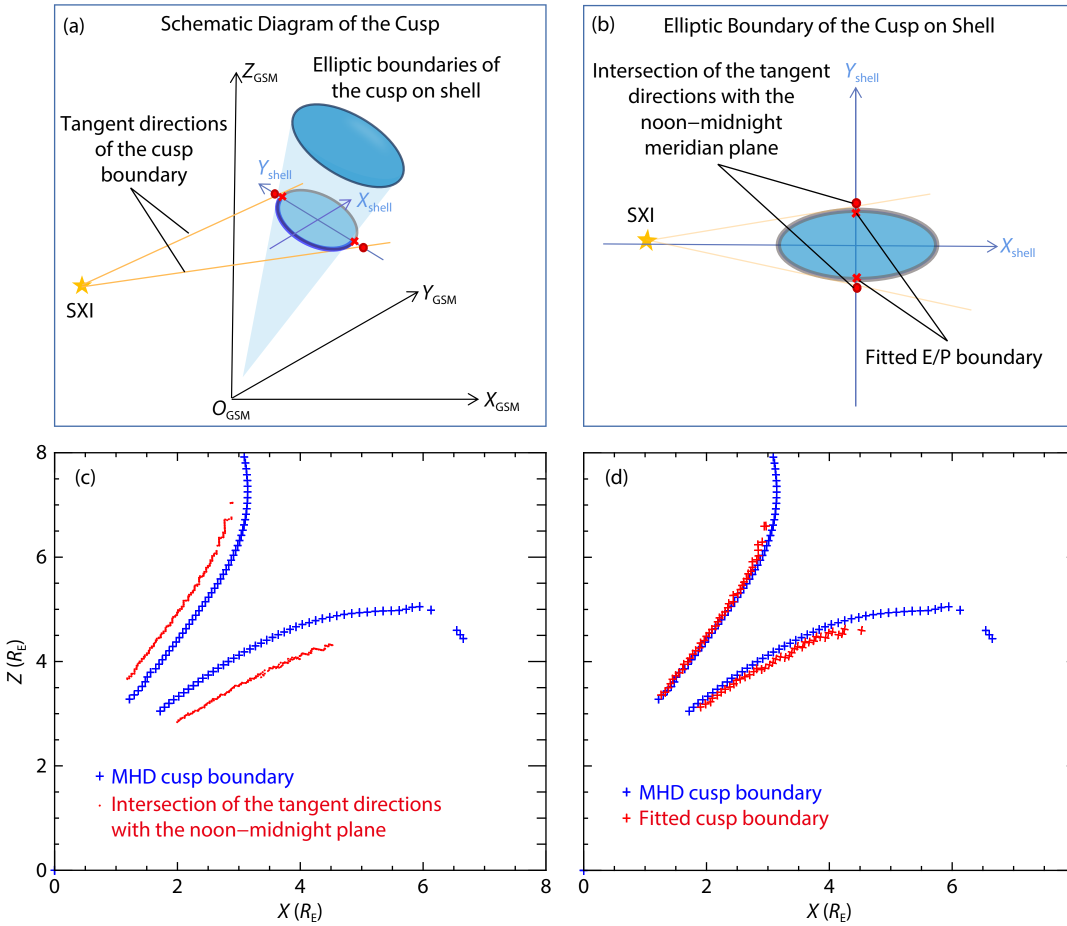

Figure 2. (a) Schematic diagram of the cusp region in the GSM coordinate system. The yellow star represents the SXI instrument; the blue 3D cone is the cusp region; and a shell coordinate system, XOY_{shell}, is used to describe the elliptic boundary on the shell. The origin of the coordinates is the center of the cusp; X_{shell} is the intersection line of the noon–midnight meridian plane and the shell. (b) The elliptical cusp boundary on the shell. The blue ellipses represent the MHD-simulated cusp boundary. The red dots show the intersection of the tangent directions with the noon–midnight meridian plane; the red crosses indicate the fitted cusp boundary. (c) The MHD cusp boundary and the intersection of the tangent directions with the noon–midnight meridian plane. (d) The MHD cusp boundary and the fitted cusp boundary.

at a given altitude, with variables that are allowed to float. In this way, an ensemble of possible cusp positions is obtained, and the tangent direction for each possible cusp can be calculated. These tangent directions are compared with those derived directly from the X-ray image to find an optimal match. Finally, the cusp morphology that has the optimal match of tangent directions with the X-ray observation shows the reconstructed cusp boundary.

Nevertheless, it should also be noted that given the information on the two tangent directions, a single ellipse cannot be pinpointed at a given altitude, with two free variables floating together, *a* and *e*. Therefore, an additional assumption has to be made that the eccentricity in reality follows that in the MHD cusp. That is to say, we assume that the MHD simulation can give a good prediction of the shape of the cusp, whereas the size of the cusp is determined by the X-ray image. This is reasonable because the MHD predicts a cusp shape that is long in the azimuthal direction and short in the latitudinal direction, consistent with observations. It should also be noted that assumptions are inevitable when deriving the 3D cusp boundaries from an X-ray image, no matter what method is used. This is because the cusp boundary is a complicated 3D shape, whereas the X-ray image is 2D. In the process of observing 2D X-ray images, information is lost on one dimension—the LOS. This is similar to the reconstruction of the magnetopause discussed in Sun TR et al. (2020), where a specific shape is assumed for the magnetopause. In the absence of a sophisticated 3D model for the cusp boundary in the literature, the treatment in this work is a preliminary expediency. In follow-up works, we plan to develop a 3D functional form for the tunnel-shaped cusp based on the MHD simulations.

Poleward and equatorward boundaries are reconstructed by utilizing the method above, based on tangent directions derived from the X-ray images and the ellipse assumption. Figure 2d denotes the cusp boundaries derived from an ensemble of elliptical cusps on the shell, with tangent directions being the best match of those derived from the X-ray image. These fitted boundaries agree well with the MHD boundaries: The average discrepancy between the blue MHD boundary and the red fitted boundary is 0.05 R_E for the poleward boundary and 0.08 R_E for the equatorward boundary. This discrepancy measures the level of error introduced

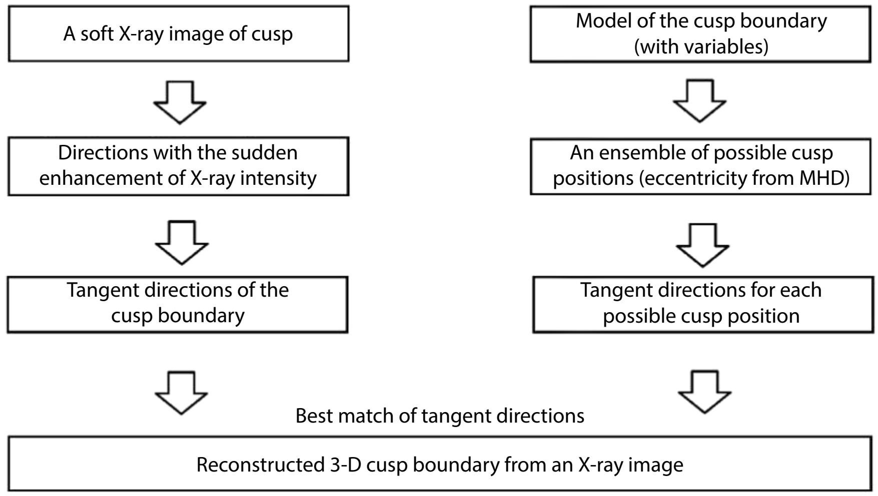

Figure 3. Flow diagram for cusp reconstruction showing the procedure used to derive the 3D position of the cusp boundary from an X-ray image.

by the method itself while assuming that the real cusp eccentricity follows the MHD; thus, by using this cusp reconstruction algorithm, it tends to be the lower limit of the discrepancy.

3.3 The Impact of IMF B_z on the Cusp Boundary

Previous observations have shown consistent and well-defined influences of IMF B_z on the poleward and equatorward boundaries of the cusp, moving equatorward under the southward IMF B_z (Newell et al., 1989; Zhou X-W et al., 1999; Pitout et al., 2006; Pitout and Bogdanova, 2021). Therefore, the validity of our method in revealing this effect has been tested in this work. This section reports our utilization of X-ray images simulated from two cases (Run 2 and Run 3 in Table 1) to delve into the impact of B_z on the cusp boundary.

In both cases, identical solar wind parameters were utilized for the MHD simulation, except for B_z values of 5 nT in Run 2 and −5 nT in Run 3. To enhance the dawn-side perspective of the cusp, the SXI position in the GSE system was set at (2.706, −7.939, 3.329) R_E, with a 60° × 60° FOV aimed toward (4.044, −0.074, 0.918) R_E. Figure 3 presents the simulation results for the cusp region under different IMF conditions.

Figures 4a1 and 4a2 present results under a northward IMF B_z (of 5 nT). Figure 4a1 displays the X-ray image and tangent directions (dotted red line), whereas Figure 4a2 depicts the MHD-determined cusp boundaries (blue crosses) and the cusp boundaries (red-cross lines) determined by the method described in Section 3.2. Figures 4b1 and 4b2 present results for a southward IMF (B_z of −5 nT). Figure 4c provides a comparison between northward (pink) and southward (bright red) IMF conditions, revealing an equatorward shift in the cusp boundary under the southward IMF, consistent with previous satellite observations and statistical findings (Newell et al., 1989; Zhou XW et al., 2000; Zong Q-G et al., 2004; Escoubet et al., 2013; Pitout and Bogdanova, 2021). Inspection of Figure 4c reveals that the poleward boundaries are apparently shifted more equatorward than the equatorward ones because the poleward-side magnetic field lines are loosely piled up, whereas the equatorward-side magnetic field is more compressed in the dayside magnetosphere.

Additionally, statistical results from Cluster data suggest that the cusp width is narrower under the southward IMF than under the northward IMF (Pitout et al., 2006). This observation is supported by the cusp width variation depicted in Figure 4c, and the reconstruction under different solar wind conditions reveals a noticeable response of the large-scale cusp structures. The upcoming SMILE satellite, scheduled for 2025, holds promise for helping further exploration of this intriguing phenomenon.

4. Tracing the Cusp Boundary in X-ray Photon Count Images

In this section, we describe the methodology by which we reconstructed the cusp boundary, using tangent directions derived from X-ray images and the ellipse boundary at a specific altitude. The investigation presented herein utilizes simulated photon count images derived from Run 1 in Table 1, in which we considered the SXI simulation with instrument effects and cosmic soft X-rays (see Section 2.2 for details). The SXI viewing geometry and solar wind conditions remain the same as those discussed in Section 3.1.

Three panels are shown in Figure 5: (a) an MHD-simulated X-ray image, namely, the X-ray intensity from the magnetosheath and cusp region simulated via the MHD code; (b) the simulated SXI photon count image derived by the instrument simulator, using only the MHD-simulated X-ray image as the input, without considering the cosmic background; and (c) the simulated SXI photon count image with the instrument effects and diffusive cosmic background considered, using the MHD-simulated X-ray image and adding the cosmic background as the input. The photon count images in Figures 5b and 5c exhibit a significant level of image noise compared with ideal X-ray images. This noise not only results in a loss of physical information, but also introduces fluctuations in the photon counts, thereby limiting the applicability of the local standard deviation method (Guo YH et al., 2022).

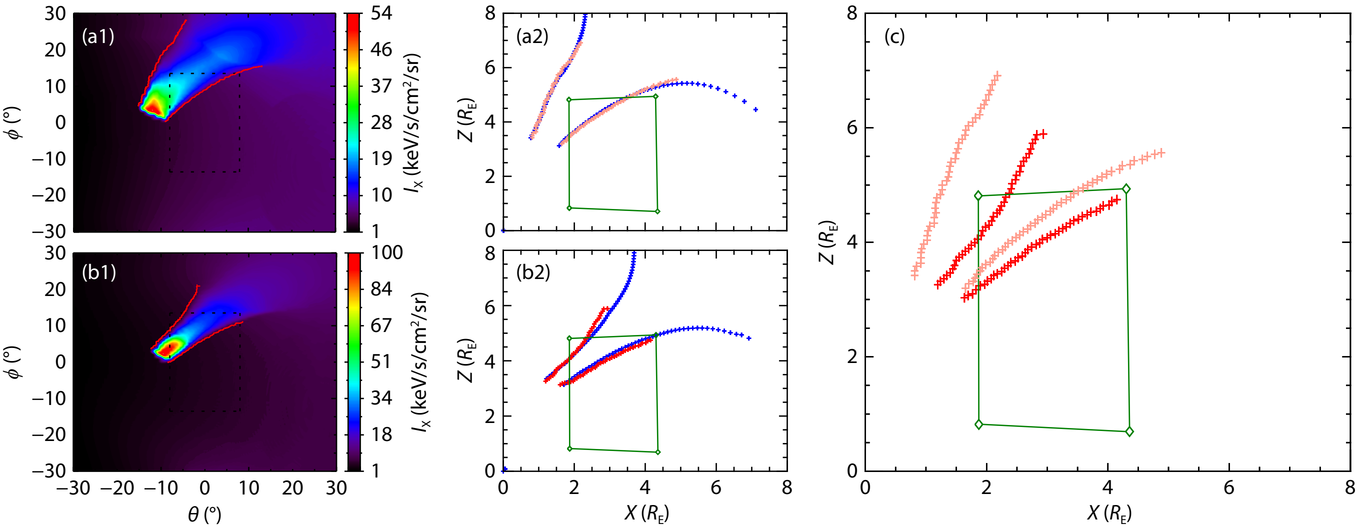

Figure 4. (a1) MHD-simulated X-ray image, and tangent directions of the cusp (red dots) with IMF B_z of 5 nT. (a2) Fitted equatorward and poleward boundaries of the cusp (pink crosses) derived by using the proposed method with IMF B_z of 5 nT. The green rectangle marks the FOV of the SXI on SMILE. (b1) MHD-simulated X-ray image and tangent directions of the cusp (red dots) with IMF B_z of −5 nT. (b2) Equatorward and poleward boundaries of the cusp (red crosses) with IMF B_z of −5 nT. (c) Comparison of cusp boundaries under IMF B_z of 5 nT (light red crosses) and −5 nT (red crosses).

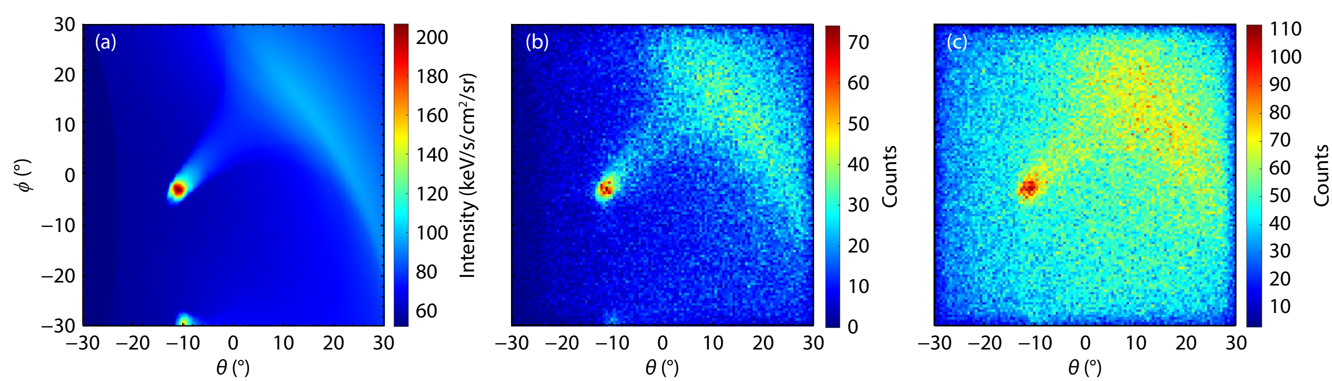

Figure 5. (a) MHD-simulated X-ray image. (b) SXI photon count image with the instrument effects. (c) SXI photon count image with the instrument effects and a diffusive cosmic background.

Consequently, a denoising step is imperative for the analysis presented in this section.

To address this, we utilized a statistically based Wiener filter to denoise the X-ray images (Khajwaniya and Tiwari, 2015; Meenakshy and Shwetha, 2015). The Wiener filter is an adaptive image denoising technique that minimizes the mean square error between the estimated and true image (Lim, 1990). For each pixel, the filter computes the local mean and variance within a defined neighborhood. It then adjusts the pixel value based on these local statistics and an estimate of the noise variance, which allows the Wiener filter to effectively suppress noise while retaining important image features such as edges and textures. To reduce noise in the X-ray images, Wiener filtering was applied independently to each of the three-color channels (red, green, and blue [RGB]) of the original RGB image. A 2D Wiener filter with a 5 × 5 neighborhood window was used for each channel. After filtering, the denoised image was produced by recombining the processed R, G, and B components.

The outcomes are demonstrated in Figure 6. The first row displays the results when only the influence of the SXI instrument effect is considered, with Figure 5b as the input figure of the denoising process. Figure 6a1 illustrates the image denoised by the Wiener filter, as well as the tangent directions of the cusp boundary (red dots) derived from the image. The absence of a color bar is due to the use of the image-processing technique, and the relative changes of X-ray intensity (instead of the absolute values) are of greater importance in deriving the cusp boundary. Figure 6a2 displays the tracing results of the cusp boundaries when using the method illustrated in Figure 3, showing a distinct difference in the growth rate of the Z value coordinate between the equatorward and poleward boundaries. The growth rate at the equatorward boundary slows down as the X value increases, whereas the poleward boundary exhibits an increasing trend, mainly because of different field line configurations near the two boundaries. Therefore, logarithmic and exponential fits are applied (indicated by the black crosses) for the fitting of poleward and equatorward bound-

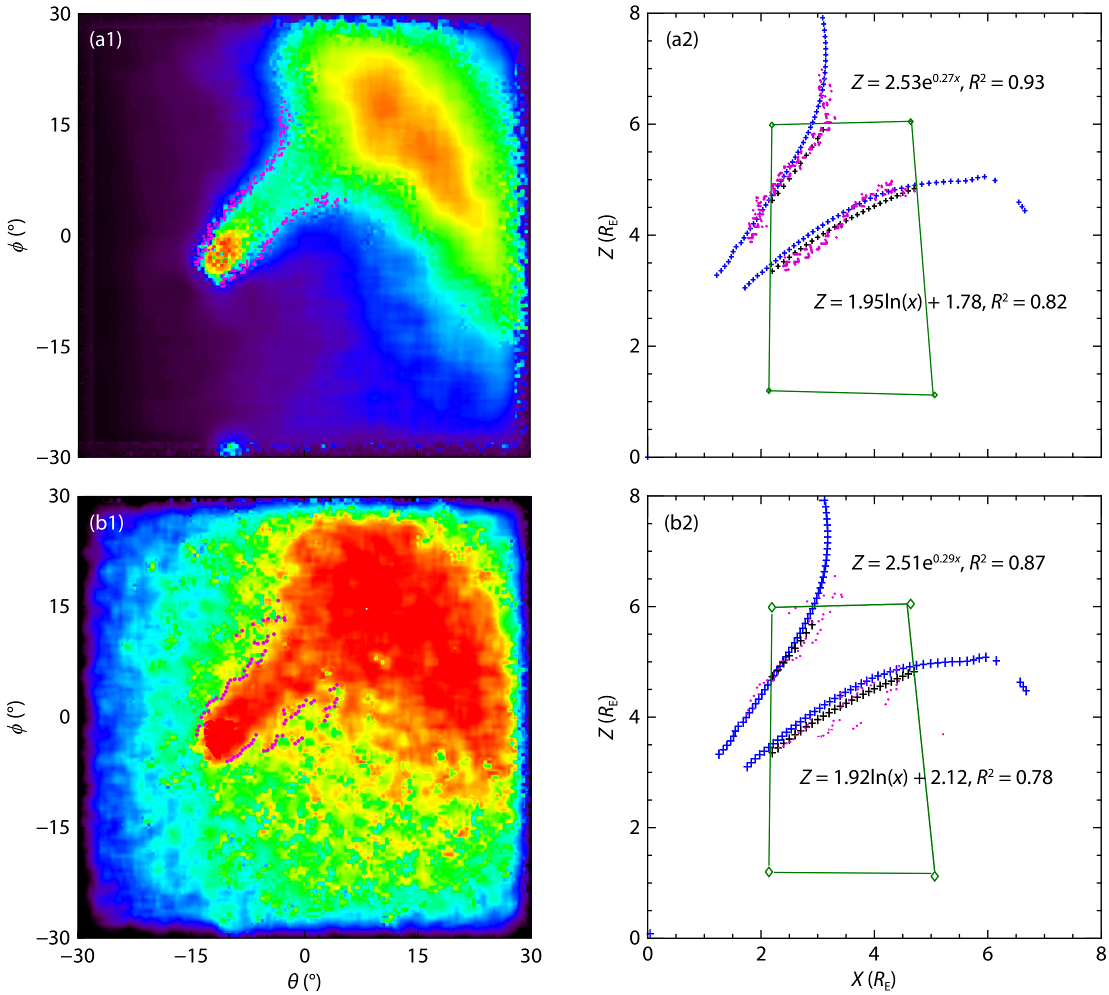

Figure 6. Cusp boundaries derived from X-ray photon count images. (a1) Denoised photon count image of Figure 5b, with the derived tangent directions of the cusp boundary shown by red dots. (a2) Comparison between the MHD cusp boundaries (blue crosses) and boundaries derived from the X-ray image, with red dots showing the equatorward and poleward boundaries derived directly from the image and black crosses outlining the shape fitted by a logarithmic function for the equatorward boundary and an exponential function for the poleward boundary. The green rectangle marks the FOV of the SXI on SMILE. (b1, b2) Denoised photon count image of Figure 5c and the derived cusp boundaries, with similar formats as (a1) and (a2).

aries, respectively. Accuracy between the fitting results (black crosses) and the MHD cusp boundary (blue crosses) thus achieved 0.26 R_E for the poleward boundary and 0.21 R_E for the equatorward boundary.

Figures 6b1 and 6b2 demonstrate the denoised image that results when both the SXI instrument effect and the cosmic X-ray background are considered, with Figure 5c as the input figure of the denoising process. The fluctuations in the X-ray image after adding the background can be at a relatively high level and thus interfere with boundary detection. A certain degree of dispersion is visible from the red dots near the equatorial boundary in Figure 6b2. From the bottom to top pixels in Figure 6b1, we may encounter some fluctuations that are high in localized regions but that apparently deviate from the large area, with high X-ray intensity from the cusps. These points return with the local maximum of the X-ray variations and are thus eliminated before the fitting to a logarithmic function. An additional condition, a monotonic increase toward the cusp center, helps with the elimination. Reasonable results are obtained and presented by the black crosses in Figure 6b2; the final boundaries in this case have average accuracy variances of 0.31 R_E for the poleward boundary and 0.22 R_E for the equatorward boundary.

5. Conclusion and Discussion

We have developed a method for tracing the equatorward and poleward boundaries of the cusp in simulated X-ray images and photon count data. On the basis of previous work by Sun TR et al. (2021), we further introduce the three-step approach shown in Figure 3:

(1) Analyzing X-ray images to pinpoint tangent directions where a notable enhancement exists in the local standard deviation of X-ray intensity;

(2) Presuming that the cusp boundaries at various altitudes have the shape of ellipses on a spherical shell, and giving a functional form of the cusp boundary with variables. It is further assumed

that the eccentricity follows the MHD results and that the size of the cusp could float. The tangent directions for each possible morphology of the cusp are calculated; and

(3) Comparing the tangent directions obtained from an X-ray image and those from possible cusp morphologies. The one returning the optimal match defines the reconstructed cusp boundary.

The validity of this method was tested with a viewing geometry when SMILE was located on the dawn side. The equatorward and poleward boundaries of the cusp were effectively reconstructed. With instrument effects and diffusive cosmic X-ray background considered, we conducted image denoising and post-reconstruction function fitting. The cusp derived boundaries were cross-compared with MHD-simulated boundaries of the cusp, and the results demonstrated that the application of this method holds promise for deriving the boundaries of the cusp from X-ray images to be observed by SMILE.

This article has focused on analyzing simulated X-ray images and photon count images for pure B_z components. The methodology also has the potential for extension to include the effects of IMF B_y and dipolar tilt on the cusp location. Regardless, additional assumptions have to be included to derive the 3D cusp from a 2D X-ray image. For instance, Zhang B et al. (2013) derived a linear regression relation between IMF B_y and MLT by using the magnetic depression method from the MHD simulation, which has enabled us to assume that the center of the cusp is located in the meridian plane at the corresponding MLT. As a result of this relationship, the proposed method for tracing the cusp boundary can potentially be extended to non-zero IMF B_y scenarios. Previous studies have also provided empirical formulas describing the impact of dipolar tilt on the latitudinal position of the cusp (e.g., Pitout et al., 2006; Liu ZQ et al., 2012). To derive a robust method that applies to different solar wind conditions, we should try various IMF directions and carefully choose which kind of empirical relationships or reasonable assumptions should be used. In an ongoing study that follows up this work, we will update the method and systematically evaluate its application to other solar wind conditions.

Although MHD simulations are not fully equipped to capture the intricate kinetic dynamics of multicomponent plasmas, they can efficiently reproduce the large-scale characteristics of cusps, which is one of the main scientific goals of the SMILE mission. After the launch of SMILE, possible joint observations from SMILE and *in situ* satellites may provide further insights into the relationship between kinetic and large-scale phenomena in the cusp region.

To improve the accuracy of the cusp boundary reconstructed from the X-ray photon number image, it is important to denoise the SXI photon count images. In this study, we utilized a 2D Wiener filter, which has been shown to reduce image noise. Nevertheless, it is worth testing or developing more image-denoising methods in the follow-up works. Furthermore, considering the absence of a quantitative study of 3D cusp morphologies in the literature, developing a functional form for the 3D cusp in future works will assist the boundary tracing from X-ray observations.

Open Research

The data for X-ray images studied in this work can be downloaded from Zenodo (https://doi.org/10.5281/zenodo.7812962).

Acknowledgments

The authors acknowledge Y. Q. Hu for developing the MHD model. This research was primarily funded by the National Natural Science Foundation of China (NNSFC) under Grant Numbers 42322408, 42188101, and 42441809. Additional support was provided by the Climbing Program of the National Space Science Center (NSSC, Grant No. E4PD3005), as well as the Specialized Research Fund for State Key Laboratories of China. The authors also extend their deepest appreciation to the editors, Hu Sufang and Andrey Samsonov, and to our peer reviewers, whose critical insights and constructive suggestions have been instrumental in enhancing the quality of our manuscript and facilitating its successful publication. Their dedicated support and guidance have been invaluable in this endeavor.

References

André, M., and Yau, A. (1997). Theories and observations of ion energization and outflow in the high latitude magnetosphere. *Space Sci. Rev.*, *80*(1), 27–48. https://doi.org/10.1023/A:1004921619885

Bogdanova, Y., Escoubet, C. P., Fear, R., Trattner, K., Berchem, J., Fazakerley, A., and Pitout, F. (2020). Mid-altitude cusp dynamics and properties during the IMF By dominated intervals. In *EGU General Assembly 2020*. Online: European Geosciences Union. https://doi.org/10.5194/egusphere-egu2020-7443

Bogdanova, Y. V., Marchaudon, A., Owen, C. J., Dunlop, M. W., Frey, H. U., Wild, J. A., Fazakerley, A. N., Klecker, B., Davies, J. A., and Milan, S. E. (2005). On the formation of the high-altitude stagnant cusp: Cluster observations. *Geophys. Res. Lett.*, *32*(12), L12101. https://doi.org/10.1029/2005GL022813

Branduardi-Raymont, G., and Wang, C. (2024). The SMILE mission. In C. Bambi, A. Santangelo (Eds). *Handbook of X-ray and Gamma-ray Astrophysics* (pp. 1369–1390). Springer, Singapore. https://doi.org/10.1007/978-981-19-6960-7_39 https://doi.org/10.1007/978-981-19-6960-7_39

Branduardi-Raymont, G., Berthomier, M., Bogdanova, Y. V., Carter, J. A., Collier, M., Dimmock, A., Dunlop, M., Fear, R. C., Forsyth, C., … Yamauchi, M. (2021). Exploring solar–terrestrial interactions via multiple imaging observers. *Exp. Astron.*, *54*(2), 361–390. https://doi.org/10.1007/s10686-021-09784-y

Burch, J. L. (1973). Rate of erosion of dayside magnetic flux based on a quantitative study of the dependence of polar cusp latitude on the interplanetary magnetic field. *Radio Sci.*, *8*(11), 955–961. https://doi.org/10.1029/RS008i011p00955

Burch, J. L. (1988). Energetic particles and currents: Results from dynamics explorer. *Rev. Geophys.*, *26*(2), 215–228. https://doi.org/10.1029/RG026i002p00215

Cai, H. T., Ma, S. Y., Dunlop, M. W., Bogdanova, Y., Davies, J. A., and Pitout, F. (2010). Cluster observations of high-altitude cusp during multiple fast-turning IMF. *Chin. Sci. Bull.*, *55*(12), 1178–1185. https://doi.org/10.1007/s11434-009-0306-0

Cao, J. B., Leonovich, A., Zhou, G. C., Liu, Z. X., Reme, H., and Dandouras, I. (2005). A theoretic interpretation of movement of the cusp equatorward boundary. *Chin. J. Space Sci.*, *25*(5), 412–418. https://doi.org/10.1111/j.1744-7909.2005.00136.x

Cargill, P. J., Lavraud, B., Owen, C. J., Grison, B., Dunlop, M. W., Cornilleau-Wehrlin, N., Escoubet, C. P., Paschmann, G., Phan, T. D., … Nykyri, K. (2005). Cluster at the magnetospheric cusps. *Space Sci. Rev.*, *118*(1), 321–366. https://doi.org/10.1007/s11214-005-3835-0

Carter, J. A., Sembay, S., and Read, A. M. (2010). A high charge state coronal mass ejection seen through solar wind charge exchange emission as detected by XMM-Newton. *Monthly Notices of the Royal Astronomical Society*, *402*(2), 867–878. https://doi.org/10.1111/j.1365-2966.2009.15985.x

Chapman, S., and Ferraro, V. C. A. (1930). A new theory of magnetic storms. *Nature*, *126*(3169), 129–130. https://doi.org/10.1038/126129a0

Collier, M. R., and Connor, H. K. (2018). Magnetopause surface reconstruction from tangent vector observations. *J. Geophys. Res.: Space Phys.*, *123*(12), 10189–10199. https://doi.org/10.1029/2018JA025763

Connor, H. K., and Carter, J. A. (2019). Exospheric neutral hydrogen density at the nominal 10 R_E subsolar point deduced from XMM-Newton X-ray observations. *J. Geophys. Res.: Space Phys.*, *124*(3), 1612–1624. https://doi.org/10.1029/2018JA026187

Connor, H. K., Sun, T. R., Samsonov, A., Liang, J., Read, A., Li, D. L, Cucho-Padin, G., Jung, J., Bickner, B., … Wang, C. (2025). SMILE modeling working group: Modeling and analysis of X-ray and ultraviolet images of solar wind–earth interactions. *Space Sci. Rev.*, *221*, 46. https://doi.org/10.1007/s11214-025-01172-8

Cravens, T. E. (2000). Heliospheric X-ray emission associated with charge transfer of the solar wind with interstellar neutrals. *Astrophys. J.*, *532*(2), L153–L156. https://doi.org/10.1086/312574

Dunlop, M. W., Lavraud, B., Cargill, P., Taylor, M. G. G. T., Balogh, A., Réme, H., Decreau, P., Glassmeier, K. H., Elphic, R. C., ... Marchaudon, A. (2005). Cluster observations of the CUSP: Magnetic structure and dynamics. *Surv. Geophys.*, *26*(1), 5–55. https://doi.org/10.1007/s10712-005-1871-7

Escoubet, C., and Bosqued, J. M. (1989). The influence of IMF-B_z and/or AE on the polar cusp: An overview of observations from the AUREOL-3 satellite. *Planet. Space Sci.*, *37*(5), 609–626. https://doi.org/10.1016/0032-0633(89)90100-1

Escoubet, C. P., Fehringer, M., and Goldstein, M. (2001). Introduction: The Cluster mission. *Ann. Geophys.*, *19*(10–12), 1197–1200. https://doi.org/10.5194/ANGEO-19-1197-2001

Escoubet, C. P., Berchem, J., Bosqued, J. M., Trattner, K. J., Taylor, M. G. G. T., Pitout, F., Vallat, C., Laakso, H., Masson, A., … Fazakerley, A. (2008). Two sources of magnetosheath ions observed by Cluster in the mid-altitude polar cusp. *Adv. Space Res.*, *41*(10), 1528–1536. https://doi.org/10.1016/j.asr.2007.04.031

Escoubet, C. P., Berchem, J., Trattner, K. J., Pitout, F., Richard, R., Taylor, M. G. G. T., Soucek, J., Grison, B., Laakso, H., … Daly, P. (2013). Double cusp encounter by Cluster: Double cusp or motion of the cusp?. *Ann. Geophys.*, *31*(4), 713–723. https://doi.org/10.5194/angeo-31-713-2013

Frank, L. A. (1971). Plasma in the Earth's polar magnetosphere. *J. Geophys. Res.*, *76*(22), 5202–5219. https://doi.org/10.1029/JA076i022p05202

Fritz, B. A., Lessard, M. R., Dymond, K. F., Kenward, D. R., Lynch, K. A., Hecht, J. H., Clemmons, J. H., Cook, T., Chakrabarti, S., and Solomon, S. C. (2020). RENU2 UV PMT observations of the cusp. *Geophys. Res. Lett.*, *47*(20), e2019GL082314. https://doi.org/10.1029/2019GL082314

Fritz, T. A., and Zong, Q. G. (2005). The magnetospheric cusps: A summary. *Surv. Geophys.*, *26*(1), 409–414. https://doi.org/10.1007/s10712-005-1904-2

Fuselier, S. A., Petrinec, S. M., Trattner, K. J., and Peterson, W. K. (2001). O^+ observations in the cusp: Implications for dayside magnetic field topology. *J. Geophys. Res.: Space Phys.*, *106*(A4), 5977–5986. https://doi.org/10.1029/2000JA003030

Fuselier, S. A., Dayeh, M. A., Galli, A., Funsten, H. O., Schwadron, N. A., Petrinec, S. M., Trattner, K. J., McComas, D. J., Burch, J. L., … Strangeway, R. J. (2020). Neutral atom imaging of the solar wind-magnetosphere-exosphere interaction near the subsolar magnetopause. *Geophys. Res. Lett.*, *47*(19), e2020GL089362. https://doi.org/10.1029/2020GL089362

Fujimoto, R., Mitsuda, K., McCammon, D., Takei, Y., Bauer, M., Ishisaki, Y., Porter, F. S., Yamaguchi, H., Hayashida, K., and Yamasaki, N. Y. (2007). Evidence for solar-wind charge-exchange X-ray emission from the Earth's magnetosheath. *Publications of the Astronomical Society of Japan*, *59*(sp1), S133–S140. https://doi.org/10.1093/pasj/59.sp1.S133

Grandin, M., Connor, H. K., Hoilijoki, S., Battarbee, M., Pfau-Kempf, Y., Ganse, U., Papadakis, K., and Palmroth, M. (2024). Hybrid-Vlasov simulation of soft X-ray emissions at the Earth's dayside magnetospheric boundaries. *Earth Planet. Phys.*, *8*(1), 70–88. https://doi.org/10.26464/epp2023052

Guo, J., Sun, T. R., Lu, S., Lu, Q. M., Lin, Y., Wang, X. Y., Wang, C., Wang, R. S., and Huang, K. (2024). Global hybrid simulations of soft X-ray emissions in the Earth's magnetosheath. *Earth Planet. Phys.*, *8*(1), 47–58. https://doi.org/10.26464/epp2023053

Guo, Y. H., Sun, T. R., Wang, C., and Sembay, S. (2022). Deriving the magnetopause position from wide field-of-view soft X-ray imager simulation. *Sci. China Earth Sci.*, *65*(8), 1601–1611. https://doi.org/10.1007/s11430-021-9937-y

Heikkila, W. J., and Winningham, J. D. (1971). Penetration of magnetosheath plasma to low altitudes through the dayside magnetospheric cusps. *J. Geophys. Res.*, *76*(4), 883–891. https://doi.org/10.1029/JA076i004p00883

Hu, Y. Q., Guo, X. C., and Wang, C. (2007). On the ionospheric and reconnection potentials of the earth: Results from global MHD simulations. *J. Geophys. Res.: Space Phys.*, *112*(A7), A07215. https://doi.org/10.1029/2006JA012145

Jorgensen, A. M., Sun, T. R., Wang, C., Dai, L., Sembay, S., Zheng, J. H., and Yu, X. Z. (2019). Boundary detection in three dimensions with application to the SMILE mission: The effect of model-fitting noise. *J. Geophys. Res.: Space Phys.*, *124*(6), 4341–4355. https://doi.org/10.1029/2018JA026124

Jorgensen, A. M., Xu, R., Sun, T., Huang, Y., Li, L., Dai, L., and Wang, C. (2022). A theoretical study of the tomographic reconstruction of magnetosheath X-ray emissions. *J. Geophys. Res.: Space Phys.*, *127*(4), e2021JA029948. https://doi.org/10.1029/2021JA029948

Khajwaniya, K. K., and Tiwari, V. (2015). Satellite image denoising using Weiner filter with SPEA2 algorithm. In *2015 IEEE 9th International Conference on Intelligent Systems and Control (ISCO)* (pp. 1–6). Coimbatore, India: IEEE. https://doi.org/10.1109/ISCO.2015.7282324

Kim, H., Connor, H. K., Jung, J., Walsh, B. M., Sibeck, D., Kuntz, K. D., Porter, F. S., Paw U, C. K., Nutter, R. A., … Collier, M. (2024). Estimating the subsolar magnetopause position from soft X-ray images using a low-pass image filter. *Earth Planet. Phys.*, *8*(1), 173–183. https://doi.org/10.26464/epp2023069

Lavraud, B., Dunlop, M. W., Phan, T. D., Rème, H., Bosqued, J. M., Dandouras, I., Sauvaud, J. A., Lundin, R., Taylor, M. G. G. T., … Balogh, A. (2002). Cluster observations of the exterior cusp and its surrounding boundaries under northward IMF. *Geophys. Res. Lett.*, *29*(20), 1995. https://doi.org/10.1029/2002GL015464

Lavraud, B., Fedorov, A., Budnik, E., Thomsen, M. F., Grigoriev, A., Cargill, P. J., Dunlop, M. W., Rème, H., Dandouras, I., and Balogh, A. (2005). High-altitude cusp flow dependence on IMF orientation: A 3-year Cluster statistical study. *J. Geophys. Res.: Space Phys.*, *110*(A2), A02209. https://doi.org/10.1029/2004JA010804

Lim, J. S. (1990). *Two-Dimensional Signal and Image Processing*. Englewood Cliffs, NJ: Prentice Hall.

Lin, R. L., Zhang, X. X., Liu, S. Q., Wang, Y. L., and Gong, J. C. (2010). A three-dimensional asymmetric magnetopause model. *J. Geophys. Res.: Space Phys.*, *115*(A4), A04207. https://doi.org/10.1029/2009JA014235

Liu, Z. Q., Lu, J. Y., Kabin, K., Yang, Y. F., Zhao, M. X., and Cao, X. (2012). Dipole tilt control of the magnetopause for southward IMF from global magnetohydrodynamic simulations. *J. Geophys. Res.: Space Phys.*, *117*(A7), A07207. https://doi.org/10.1029/2011JA017441

Liu, Z. Q., Lu, J. Y., Wang, C., Kabin, K., Zhao, J. S., Wang, M., Han, J. P., Wang, J. Y., and Zhao, M. X. (2015). A three-dimensional high Mach number asymmetric magnetopause model from global MHD simulation. *J. Geophys. Res.: Space Phys.*, *120*(7), 5645–5666. https://doi.org/10.1002/2014JA020961

Meenakshy, K., and Shwetha, C. (2015). Combined NLM-Weiner filter based image denoising. In *2015 International Conference on Power, Instrumentation, Control and Computing (PICC)* (pp. 1–3). Thrissur, India: IEEE. https://doi.org/10.1109/PICC.2015.7455801

Měrka, J., Šafránková, J., and Němeček, Z. (2002). Cusp-like plasma in high altitudes: A statistical study of the width and location of the cusp from Magion-4. *Ann. Geophys.*, *20*(3), 311–320. https://doi.org/10.5194/angeo-20-311-2002

Newell, P. T., and Meng, C. I. (1988). The cusp and the cleft/boundary layer: Low-altitude identification and statistical local time variation. *J. Geophys. Res.: Space Phys.*, *93*(A12), 14549–14556. https://doi.org/10.1029/JA093iA12p14549

Newell, P. T., Meng, C. I., Sibeck, D. G., and Lepping, R. (1989). Some low-altitude cusp dependencies on the interplanetary magnetic field. *J. Geophys. Res.:*

Space Phys., *94*(A7), 8921–8927. https://doi.org/10.1029/JA094iA07p08921
Peng, S. W., Ye, Y. Z., Wei, F., Yang, Z. H., Guo, Y. H., and Sun, T. R. (2018). Numerical model built for the simulation of the earth magnetopause by lobster-eye-type soft X-ray imager onboard SMILE satellite. *Opt. Express*, *26*(12), 15138–15152. https://doi.org/10.1364/OE.26.015138
Petrinec, S. M., Kletzing, C. A., Bounds, S. R., Fuselier, S. A., Trattner, K. J., and Sawyer, R. P. (2023). TRICE-2 rocket observations in the low-altitude cusp: Boundaries and comparisons with models. *J. Geophys. Res.: Space Phys.*, *128*(3), e2022JA030952. https://doi.org/10.1029/2022JA030952
Pitout, F., Escoubet, C. P., Klecker, B., and Rème, H. (2006). Cluster survey of the mid-altitude cusp: 1. Size, location, and dynamics. *Ann. Geophys.*, *24*(11), 3011–3026. https://doi.org/10.5194/angeo-24-3011-2006
Pitout, F., Escoubet, C. P., Klecker, B., and Dandouras, I. (2009). Cluster survey of the mid-altitude cusp – Part 2: Large-scale morphology. *Ann. Geophys.*, *27*(5), 1875–1886. https://doi.org/10.5194/angeo-27-1875-2009
Pitout, F., and Bogdanova, Y. V. (2021). The polar cusp seen by Cluster. *J. Geophys. Res.: Space Phys.*, *126*(9), e2021JA029582. https://doi.org/10.1029/2021JA029582
Reiff, P. H., Hill, T. W., and Burch, J. L. (1977). Solar wind plasma injection at the dayside magnetospheric cusp. *J. Geophys. Res.*, *82*(4), 479–491. https://doi.org/10.1029/JA082i004p00479
Russell, C. T., Chappell, C. R., Montgomery, M. D., Neugebauer, M., and Scarf, F. L. (1971). Ogo 5 observations of the polar cusp on November 1, 1968. *J. Geophys. Res.*, *76*(28), 6743–6764. https://doi.org/10.1029/JA076i028p06743
Samsonov, A., Carter, J. A., Read, A., Sembay, S., Branduardi-Raymont, G., Sibeck, D., and Escoubet, P. (2022). Finding magnetopause standoff distance using a soft X-ray imager: 1. Magnetospheric masking. *J. Geophys. Res.: Space Phys.*, *127*, e2022JA030848.
Samsonov, A., Branduardi-Raymont, G., Sembay, S., Read, A., Sibeck, D., and Rastaetter, L. (2024). Simulation of the SMILE Soft X-ray Imager response to a southward interplanetary magnetic field turning. *Earth Planet. Phys.*, *8*(1), 39–46. https://doi.org/10.26464/epp2023058
Sawyer, R. P., Fuselier, S. A., Kletzing, C. A., Bonnell, J. W., Roglans, R., Bounds, S. R., Kim, M. J., Vines, S. K., Cairns, I. H., … George, D. (2021). TRICE 2 observations of low-energy magnetospheric ions within the cusp. *J. Geophys. Res.: Space Phys.*, *126*(9), e2021JA029382. https://doi.org/10.1029/2021JA029382
Scarf, F. L., Fredricks, R. W., Green, I. M., and Russell, C. T. (1972). Plasma waves in the dayside polar cusp: 1, Magnetospheric observations. *J. Geophys. Res.*, *77*(13), 2274–2293. https://doi.org/10.1029/JA077i013p02274
Sembay, S., Alme, A. L., Agnolon, D., Arnold, T., Beardmore, A., Margeli, A. B. B., Bicknell, C., Bouldin, C., Branduardi-Raymont, G., … Yang, S. (2024). The Soft X-ray Imager (SXI) on the SMILE mission. *Earth Planet. Phys.*, *8*(1), 5–14. https://doi.org/10.26464/epp2023067
Sibeck, D. G., Collier, M. R., and Silveira, M. V. D. (2021). Neutral densities in the outer exosphere near the subsolar magnetopause. *Geophys. Res. Lett.*, *48*(23), e2021GL093383. https://doi.org/10.1029/2021GL093383
Sun, T. R., Wang, C., Wei, F., and Sembay, S. (2015). X-ray imaging of Kelvin-Helmholtz waves at the magnetopause. *J. Geophys. Res.: Space Phys.*, *120*(1), 266–275. https://doi.org/10.1002/2014JA020497
Sun, T. R., Wang, C., Sembay, S. F., Lopez, R. E., Escoubet, C. P., Branduardi-Raymont, G., Zheng, J. H., Yu, X. Z., Guo, X. C., … Guo, Y. H. (2019). Soft X-ray imaging of the magnetosheath and cusps under different solar wind conditions: MHD simulations. *J. Geophys. Res.: Space Phys.*, *124*(4), 2435–2450. https://doi.org/10.1029/2018JA026093
Sun, T. R., Wang, C., Connor, H. K., Jorgensen, A. M., and Sembay, S. (2020). Deriving the magnetopause position from the soft X-ray image by using the tangent fitting approach. *J. Geophys. Res.: Space Phys.*, *125*(9), e2020JA028169. https://doi.org/10.1029/2020JA028169
Sun, T. R., Wang, X., and Wang, C. (2021). Tangent directions of the cusp boundary derived from the simulated soft X-ray image. *J. Geophys. Res.: Space Phys.*, *126*(3), e2020JA028314. https://doi.org/10.1029/2020JA028314
Trattner, K. J., Fuselier, S. A., Peterson, W. K., and Carlson, C. W. (2002). Spatial features observed in the cusp under steady solar wind conditions. *J. Geophys. Res.: Space Phys.*, *107*(A10), 1288. https://doi.org/10.1029/2001JA000262
Trattner, K. J., Fuselier, S. A., Petrinec, S. M., Yeoman, T. K., Mouikis, C., Kucharek, H., and Rème, H. (2005). Reconnection sites of spatial cusp structures. *J. Geophys. Res.: Space Phys.*, *110*(A4), A04207. https://doi.org/10.1029/2004JA010722
Trattner, K. J., Petrinec, S. M., Fuselier, S. A., Nykyri, K., and Kronberg, E. (2011). Cluster observations of bow shock energetic ion transport through the magnetosheath into the cusp. *J. Geophys. Res.: Space Phys.*, *116*(A9), A09207. https://doi.org/10.1029/2011JA016617
Tsyganenko, N. A., and Russell, C. T. (1999). Magnetic signatures of the distant polar cusps: Observations by Polar and quantitative modeling. *J. Geophys. Res.: Space Phys.*, *104*(A11), 24939–24955. https://doi.org/10.1029/1999JA900279
Wang, C., Li, Z. J., Sun, T. R., Liu, Z. Q., Liu, J., Wu, Q., Zheng, J. H., and Li, J. (2017). SMILE satellite mission survey. *Space Int. (in Chinese)*, (8), 13–16. https://doi.org/10.3969/j.issn.1009-2366.2017.08.003
Wang, C., and Sun, T. R. (2022). Methods to derive the magnetopause from soft X-ray images by the SMILE mission. *Geosci. Lett.*, *9*(1), 30. https://doi.org/10.1186/s40562-022-00240-z
Wang, C., Branduardi-Raymont, G., Escoubet, C. P., and Forsyth, C. (2025). Solar wind Magnetosphere Ionosphere Link Explorer (SMILE): Science and mission overview. *Space Sci. Rev.*, *221*, 9. https://doi.org/10.1007/s11214-024-01126-6
Watermann, J., Lühr, H., Schlegel, K., Stauning, P., Thayer, J. P., Christiansen, F., and Newell, P. T. (2005). The low-altitude cusp: Multi-point observations during the February 2002 SIRCUS campaign. In C. Reigber, et al. (Eds.), *Earth Observation with CHAMP: Results from Three Years in Orbit* (pp. 375–380). Berlin: Springer. https://doi.org/10.1007/3-540-26800-6_60
Xiao, C., Liu, W. L., Shen, C., Zhang, H., and Rong, Z. J. (2018). Study on the curvature and gradient of the magnetic field in Earth's cusp region based on the magnetic curvature analysis method. *J. Geophys. Res.: Space Phys.*, *123*(5), 3794–3805. https://doi.org/10.1029/2017JA025028
Xu, J. Y., Lü, J. Y., Wang, M., and Guo, J. G. (2018). Cusp location dependence on IMF: Cluster statistical study. *Chinese J. Geophys. (in Chinese)*, *61*(9), 3526–3535. https://doi.org/10.6038/cjg2018M0118
Yang, Z. W., Jarvinen, R., Guo, X. C., Sun, T. R., Koutroumpa, D., Parks, G. K., Huang, C., Tang, B. B., Lu, Q. M., and Wang, C. (2024). Deformations at Earth's dayside magnetopause during quasi-radial IMF conditions: Global kinetic simulations and Soft X-ray Imaging. *Earth Planet. Phys.*, *8*(1), 59–69. https://doi.org/10.26464/epp2023059
Zhang, B., Brambles, O., Lotko, W., Dunlap-Shohl, W., Smith, R., Wiltberger, M., and Lyon, J. (2013). Predicting the location of polar cusp in the Lyon-Fedder-Mobarry global magnetosphere simulation. *J. Geophys. Res.: Space Phys.*, *118*(10), 6327–6337. https://doi.org/10.1002/jgra.50565
Zhang, Y. J., Sun, T. R., Wang, C., Ji, L., Carter, J. A., Sembay, S., Koutroumpa, D., Liu, Y. D., Liang, G. Y., … Zhao, X. W. (2022). Solar wind charge exchange soft X-ray emissions in the magnetosphere during an interplanetary coronal mass ejection compared to its driven sheath. *Astrophys. J. Lett.*, *932*(1), L1. https://doi.org/10.3847/2041-8213/ac7521
Zhou, X. W., Russell, C. T., Le, G., Fuselier, S. A., and Scudder, J. D. (2000). Solar wind control of the polar cusp at high altitude. *J. Geophys. Res.: Space Phys.*, *105*(A1), 245–251. https://doi.org/10.1029/1999JA900412
Zoennchen, J. H., Bailey, J. J., Nass, U., Gruntman, M., Fahr, H. J., and Goldstein, J. (2011). The TWINS exospheric neutral H-density distribution under solar minimum conditions. *Ann. Geophys.*, *29*(12), 2211–2217. https://doi.org/10.5194/angeo-29-2211-2011
Zong, Q.-G., Fritz, T. A., Zhang, H., Korth, A., Daly, P. W., Dunlop, M. W., Glassmeier, K. H., Reme, H., and Balogh, A. (2004). Triple cusps observed by Cluster—Temporal or spatial effect?. *Geophys. Res. Lett.*, *31*(9), L09810. https://doi.org/10.1029/2003GL019128
Zong, Q.-G., Zhang, H., Fritz, T. A., Goldstein, M. L., Wing, S., Keith, W., Winningham, J. D., Frahm, R., Dunlop, M. W., … Fazakerley, A. N. (2008). Multiple cusps during an extended northward IMF period with a significant B_y component. *J. Geophys. Res.: Space Phys.*, *113*(A1), A01210. https://doi.org/10.1029/2006JA012188
Zhou, X.-W., Russell, C. T., Le, G., Fuselier, S. A., and Scudder, J. D. (1999). The polar cusp location and its dependence on dipole tilt. *Geophysical Research Letters*, *26*(3), 429–432. https://doi.org/10.1029/1998GL900312